

The X-Ray Structure of the Supernova Remnant 3C 400.2

Kumi YOSHITA, Hiroshi TSUNEMI, Emi MIYATA, and Koji MORI

Department of Earth and Space Science, Graduate School of Science, Osaka University

1-1 Machikaneyama, Toyonaka, Osaka 560-0043

E-mail(KY): kyoshita@ess.sci.osaka-u.ac.jp

(Received 2000 June 26; accepted 2000 October 24)

Abstract

We present here the results of an X-ray study of the supernova remnant 3C 400.2 (G53.6–2.2) using the ASCA data. 3C 400.2 has an unusual morphology at radio wavelengths, suggesting two SNRs superposed along the same line of sight, whereas its X-ray emission is known to be centrally peaked. We investigated the X-ray spectral variation across the remnant using the ASCA GIS and the ROSAT PSPC data. The X-ray spectra can be well fitted by thin thermal plasma models. However, there is no significant variation in the temperature and the ionization parameter across the remnant. We conclude that it is a single SNR rather than two overlapping SNRs. The centrally peaked X-ray morphology and the thin thermal emission with nearly cosmic abundances indicate that 3C 400.2 belongs to a class of “mixed-morphology SNRs”. We found that the physical parameters of 3C 400.2 are similar to those of other mixed-morphology SNRs. The morphology of 3C 400.2 can be explained by a supernova explosion occurring near to the edge of an interstellar cloud.

Key words: ISM: individual (3C 400.2) — supernova remnants — X-rays: ISM

1. Introduction

The supernova remnant (SNR) 3C 400.2 is known to have an unusual morphology in the radio band. With the VLA observations at 327.5 and 1465 MHz, Dubner (1994) reported two circular shells that overlap each other, from which one might imagine two interacting SNRs. The larger shell has a diameter of 22' centered near $(\alpha, \delta)(J2000) = (19^{\text{h}}38^{\text{m}}53^{\text{s}}, 17^{\circ}13')$. The other shell is 14' in diameter, whose center is almost at the northwestern edge of the larger shell, $(\alpha, \delta)(J2000) = (19^{\text{h}}38^{\text{m}}09^{\text{s}}, 17^{\circ}18')$. Goss et al. (1975) found that the spectral index in radio flux, S , has no difference between two shells with $\alpha = -0.62 \pm 0.04$, where $S = \nu^\alpha$.

The X-ray emission from 3C 400.2 was first detected with HEAO 1 (Agrawal et al. 1983). The Einstein IPC observation showed that the X-ray emission fills the interior of the radio shell (Long et al. 1991). This leads to the fact that 3C 400.2 belongs to a group of SNRs which have a limb-brightened radio and centrally peaked X-ray morphology. The X-ray peak is located in the region where the radio shells overlap each other. The ROSAT PSPC spectrum could be fitted by a thin thermal plasma model (Saken et al. 1995). They found a small increase of the hardness ratio in the X-ray bright region, although the values of the column density and the electron temperature were highly correlated.

Optically, 3C 400.2 can be described as an incomplete

shell structure of diffuse filaments with a diameter of 16' (Winkler et al. 1993). It is smaller than the radio shell. Although the optical shell is located at a region with high surface brightness on the western side of the radio shells, there is little correlation among the three images at the optical, radio, and X-ray wavelengths.

The distance to 3C 400.2 remains uncertain. Case and Bhattacharya (1998) derived a distance of 5.0 kpc from the systemic velocity of the optical filaments obtained in Rosado et al. (1983), using a more modern rotation curve. On the other hand, Giacani et al. (1998) estimated the distance to be 2.3 kpc based on an observation of the HI cloud toward 3C 400.2. Other distance estimates are based on the highly uncertain method of the Σ – D relation and vary from 3.8 to 6.9 kpc (Clark, Caswell 1976; Caswell, Lerche 1979; Milne 1979; Allakhverdiev 1983; Dubner et al. 1994).

Only a few examples of interacting or overlapping SNRs have been reported. Among these, two cases have been found in the Large Magellanic Cloud. One is DEM L316, which shows two overlapping shells at radio and optical wavelengths (Williams et al. 1997). The overlapping area is smaller than that of 3C 400.2, and two shells are clearly separated. Unlike 3C 400.2, there are two circular regions of the X-ray emission, corresponding to the two shells. The recent ASCA observation of DEM L316 found that the X-ray properties in two shells have different electron temperatures, ionization parameters, and

Table 1. Summary of ASCA and ROSAT observations.

Mission	Sequence number	Date of observation	Field center		Effective exposure (ks)
			α (J2000)	δ (J2000)	
ASCA	54024000	1996 Apr 13-14	19 ^h 38 ^m 34 ^s	17°23'42''	19 (GIS)
ROSAT	RP500190N00	1992 Oct 4-10	19 ^h 38 ^m 24 ^s	17°19'48''	3.6

elemental abundances (Nishiuchi et al. 2001). They concluded that DEM L316 is surely two SNRs. The other is the SNR N186D, which is believed to be interacting with the N186E region (Rosado et al. 1990). They suggest that N186E is an old SNR which is ionized by internal stars. No X-ray study of N186D has been reported (Williams et al. 1999).

In our galaxy, Yoshita et al. (2000) found that the X-ray emission extends over the radio shell of the known radio SNR G69.7+1.0. They suggest that the X-ray emission comes from a different SNR, G69.4+1.2, which has a shell of 1° diameter at radio and optical wavelengths. In this case, the large shell of G69.4+1.2 surrounds a radio shell of G69.7+1.0 with 16' diameter, and are overlapping. A similar situation has been found in the region of CTB 1 (G116.9+0.2) by Craig et al. (1997). They suggest that the limb-like X-ray emission surrounding CTB 1 may be a previously unknown SNR, G117.7+0.6.

In this paper, we report on an X-ray study of 3C 400.2 using the ASCA data. With only the ROSAT PSPC data, the obtained parameters were the column density and the electron temperature, which were strongly coupled. The high-energy resolution of ASCA allowed us to determine the elemental abundances as well as the ionization parameter of the plasma. Although the spatial resolution of ASCA is about 3', it is possible to search for the spectral variation across 3C 400.2, owing to its angular size of 33' × 28'. We also used the ROSAT PSPC data to cover the low-energy band.

2. Observations of 3C 400.2

We retrieved the ASCA and the ROSAT data of 3C 400.2 from the HEASARC (High Energy Astrophysics Science Archive Research Center) public databases. The ASCA observation was carried out on 1996 April 13 with the two Solid-state Imaging Spectrometers (SIS 0 and SIS 1) and the two Gas Imaging Spectrometers (GIS 2 and GIS 3). The SIS data were taken in 2-CCD BRIGHT mode whose field of view (FOV) is 11' × 22', while the GISs have a larger FOV of 50' in diameter.

Both the GIS data and the SIS data were screened based on the following criteria. We rejected events recorded in the South Atlantic Anomaly (SAA) and the

high-background regions with the geomagnetic cut-off rigidity of < 6 GV. The screening criterion for the angle between the rim of the Earth and the pointing direction was < 5° when the Earth rim is dark, and it < 25° for the GIS, < 40° for the SIS 0 and < 20° for the SIS 1, when the rim of the Earth is bright. For the GIS data, we applied a “flare-cut” to maximize the signal-to-noise ratio, as described in Ishisaki et al. (1997). The SIS data were corrected for the charge-transfer inefficiency (Dotani et al. 1995, 1997), and hot and flickering pixels were removed using the standard procedures. The effective exposure times were 19 ks for GIS 2 and GIS 3 and 22 ks for SIS 0, 24 ks for SIS 1.

We also analyzed the ROSAT PSPC data of 3C 400.2. We used the basic science data of sequence RP500190N00, which has already been analyzed by Saken et al. (1995). This observation was performed on 1992 October 4–10 and the exposure was 3.6 ks. A summary of the ASCA and ROSAT observations which we analyzed is given in table 1.

3C 400.2 is located at $(l, b) = (53^{\circ}6, -2^{\circ}2)$, far from the galactic center. In addition, the angular distance from the galactic plane is larger than the scale height of the galactic ridge emission of ~ 100 pc (0.67 at 8.5 kpc; Yamauchi et al. 1993). Therefore, we considered the galactic ridge emission to be negligible. We treated only two components as the GIS background: the non-X-ray background (NXB) and the uniform cosmic X-ray background (CXB). For the GIS, the NXB data were reproduced using a method introduced by Ishisaki (1996), and the CXB were estimated from the Large Sky Survey (Ueda et al. 1999) data. Total background data consisting of the NXB and CXB were subtracted from the GIS data. For the SIS, we considered the blank-sky (north ecliptic pole and Lynx field regions) data as background. The background spectrum of the ROSAT PSPC was extracted from the regions outside the remnant.

We generated exposure-corrected, background-subtracted images of the GIS. Figure 1 shows a GIS image of 3C 400.2 in gray scale superposed on the VLA contour map at 1.4 GHz. The VLA image was obtained through Skyview supported by HEASARC/GSFC. A centrally peaked and elliptical X-ray morphology is clearly seen.

Based on a radio-intensity map, we delineated the two shells by the regions indicated by the solid circles in fig-

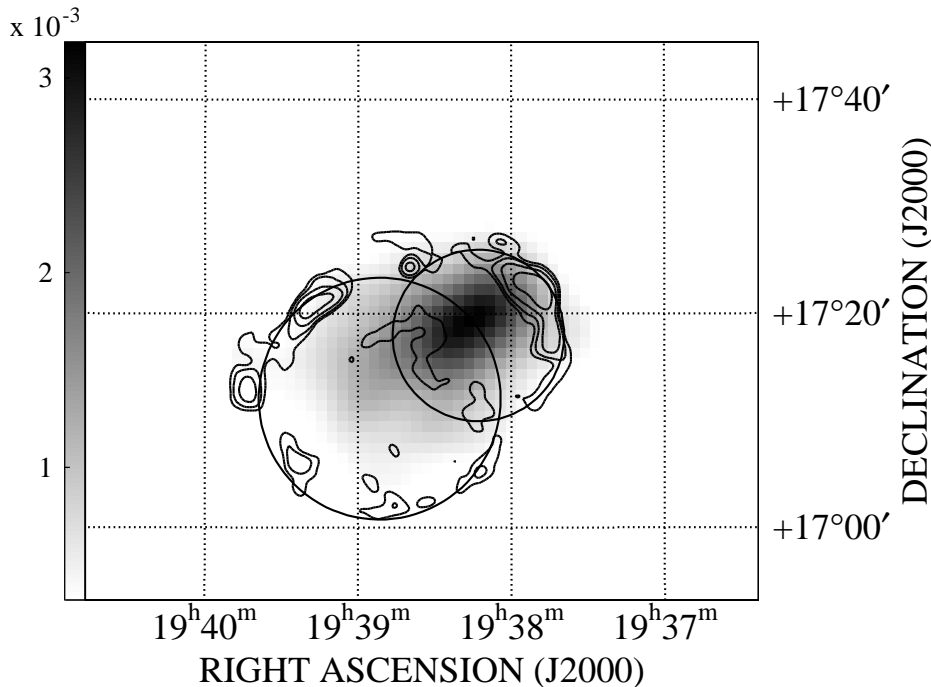


Fig. 1. ASCA GIS image of 3C 400.2. The contours are the VLA image at 1.4 GHz. The contour levels are 0.5, 1, 2, 4, 8 in units of mJy/beam. The two circles based on the radio intensity are indicated by solid lines. The circles are 16'3 and 23'0 in diameter.

ure 1. As noted earlier, the shells overlap. The smaller shell in the NW has a diameter of 16'3, while the larger one in the SE has a diameter of 23'0. The X-ray surface brightness becomes the maximum inside the NW shell, which is consistent with previous observations (Long et al. 1991; Saken et al. 1995).

3. Spectral Results

We searched for spectral variation over 3C 400.2. We divided the remnant into three regions: the overlapping region of two shells (center), and the remaining parts of the NW shell (NW) and the SE shell (SE). Figure 2 shows the regions where we extracted the spectra. The SIS FOV is also shown by the two boxes in figure 2. They covered only part of the remnant. Therefore, we cannot use the SIS data for studying the spectral variation. Since the GIS is sensitive only above 0.7 keV, we used the ROSAT PSPC data to cover the low-energy band.

There is a point source of an F8 star seen in the PSPC image of 3C 400.2 (Saken et al. 1995) which is not seen in our GIS data. We excluded the region of the F8 star from our spectral analysis in the data screening for the GIS as well as the PSPC in order to avoid contamination. In figure 2, the circle, 4' in diameter, in the southeast of

the remnant indicates the excluded region.

In addition, we excluded the southeastern part of the SE shell. Because this region corresponds to the edge of the GIS FOV, the background is high and the gain is uncertain. We picked up the events within the 21' radius from the center of the GIS FOV.

The extracted spectra through this process were binned in such a way that each channel contained more than 20 counts to apply the χ^2 test. The background-subtracted spectra are shown in figure 3. We performed a simultaneous fit of all three sets of data (GIS 2, GIS 3, and PSPC data) using XSPEC (V10.0). The Si lines seen in the spectra indicate that the X-ray emission surely arises from a hot, thermal plasma, as had been suggested by previous analyses (Long et al. 1991; Saken et al. 1995). First, we applied a collisional ionization equilibrium (CIE) model (MEKAL model, Mewe et al. 1985; Liedahl et al. 1995) with cosmic abundances (Anders, Grevesse et al. 1989) to the spectra. We employed the model of Morrison and McCammon (1983) as the interstellar absorption feature. Acceptable fits were obtained in the NW and SE, but not for the “center region”; $\chi^2/\text{d.o.f} = 176.3/138$ where d.o.f. stands for the degrees of freedom. There are large residuals around 1.2 keV which are thought to be due to an improper fit to the

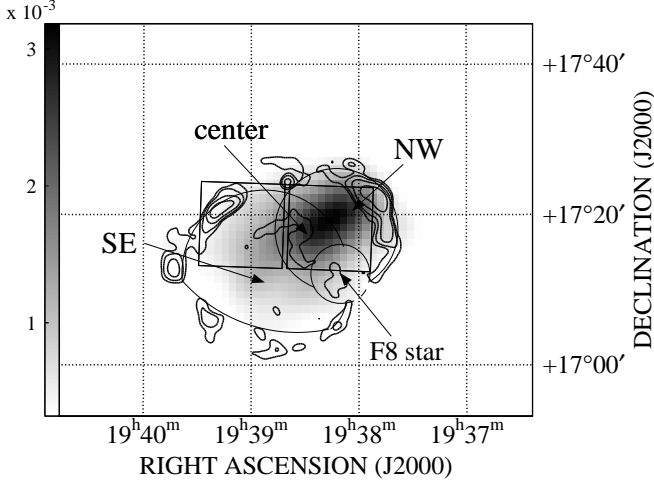


Fig. 2. Same as figure 1, but showing various regions used in the spectral analysis. The thick lines indicate three regions (SE, center, NW) where the GIS and PSPC spectra are extracted. The data within the circle in the southeast are excluded so as to avoid any contamination by the F8 star which was detected with the ROSAT. The SIS FOV is indicated by two boxes.

Fe-L line blends.

In order to improve this, we further attempted two cases: one is to leave the Fe abundance free (Case 1), and the other is to introduce the non-equilibrium ionization (NEI) model (Case 2). We employed a VMEKAL model in case 1 and the NEI model coded by Masai (1984) in case 2, respectively. The fitting results for the two cases are listed in table 2, where the errors quoted are at the 90% confidence level. Both cases reduced the value of χ^2 . In particular, case 2 reduced the χ^2 value for the “center region” by ~ 30 , which resulted in acceptable fits. The ionization parameter of $\log(\tau) \sim 11$ obtained in case 2 indicates that plasmas have not reached the ionization equilibrium over the entire remnant. This is consistent with the low electron density derived in the following section, in spite of the old age expected from the optical filaments and the low electron temperature.

Finally, we applied the NEI model, allowing the abundance of Fe to be free parameters (Case 3). The best-fit results summarized in table 2 are shown by the solid lines in figure 3. We found no significant variation of any parameters, column density (N_H), electron temperature (kT_e), ionization parameter [$\log(\tau)$], within the statistical uncertainties over the entire remnant. The abundance of Fe shows a slight enhancement in the “center region”.

Table 3 summarizes the emission measures ($n_e^2 L$ where L is the depth of the plasma) for three regions which are calculated using the results for GIS in case 3. We fixed the kT_e value when we derived the error range of the

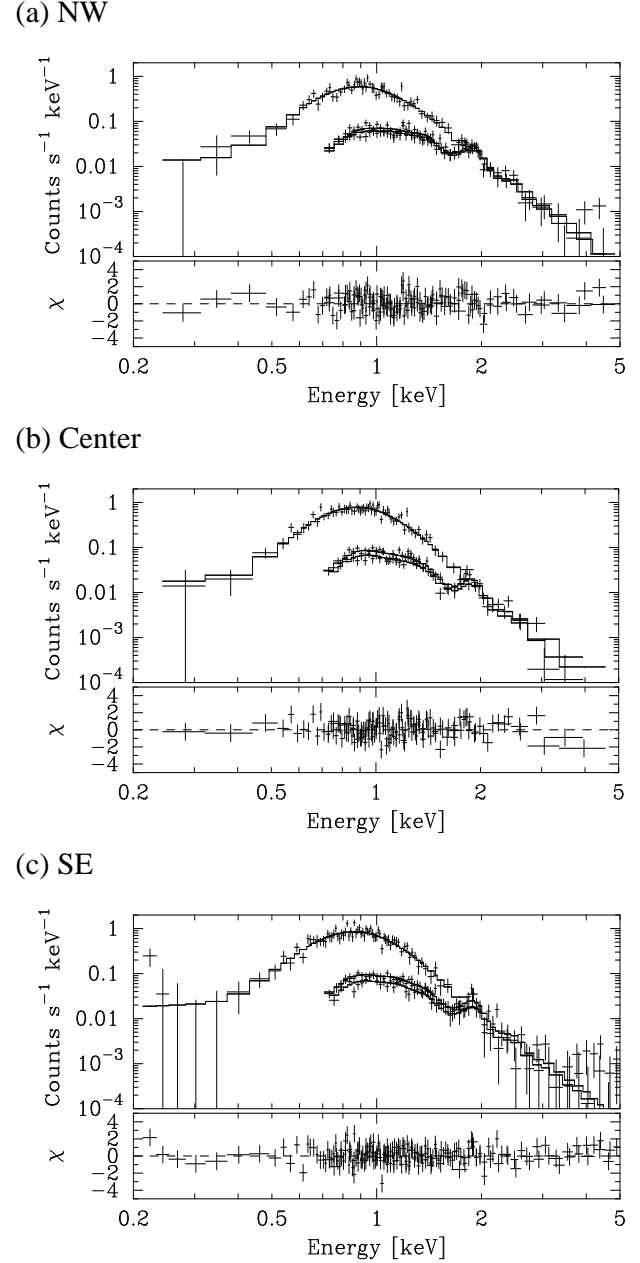


Fig. 3. GIS 2, GIS 3, and PSPC spectra from three regions of 3C 400.2. In each figure, the solid line is the best-fit model of case 3 (see table 2) and the residuals of the fit are shown in the lower panel.

$n_e^2 L$. The ratio of $n_e^2 L$ between SE and other regions is also given in table 3. The $n_e^2 L$ value tends to be larger from the southeast to the northwest.

We also performed the spectral fitting with the model of case 3 including the SIS data. We have extracted the spectra for three instruments (SIS, GIS, and PSPC) from the region corresponding to the

Table 2. Best-fit results for each region of 3C400.2. The errors are at the 90% confidence levels.

Region	$\chi^2/\text{d.o.f}$	N_{H} [10^{21}cm^{-2}]	kT_e [keV]	$\log \tau$	Fe
Case 1					
NW	163.4/150	4.5 ± 1.3	$0.56^{+0.06}_{-0.05}$...	$0.8^{+0.4}_{-0.3}$
center	169.1/137	$4.3^{+1.1}_{-1.2}$	$0.58^{+0.05}_{-0.06}$...	$1.7^{+0.6}_{-0.4}$
SE	169.9/185	3.5 ± 1.2	$0.53^{+0.06}_{-0.07}$...	$1.3^{+0.5}_{-0.3}$
Case 2					
NW	153.1/150	$6.2^{+0.9}_{-1.3}$	$0.75^{+0.16}_{-0.13}$	10.7 ± 0.3	...
center	146.8/137	$4.7^{+1.2}_{-2.0}$	$0.54^{+0.12}_{-0.08}$	11.2 ± 0.3	...
SE	158.2/185	$4.9^{+0.7}_{-1.4}$	$0.62^{+0.17}_{-0.12}$	$10.8^{+0.4}_{-0.3}$...
Case 3					
NW	153.0/149	$6.2^{+0.9}_{-1.3}$	$0.76^{+0.22}_{-0.15}$	10.7 ± 0.3	$1.0^{+0.4}_{-0.3}$
center	134.9/136	$4.4^{+1.5}_{-1.3}$	$0.80^{+0.23}_{-0.20}$	$10.9^{+0.3}_{-0.2}$	$2.0^{+0.6}_{-0.5}$
SE	154.8/184	$4.8^{+0.8}_{-1.4}$	$0.83^{+0.44}_{-0.24}$	10.6 ± 0.3	$1.4^{+0.6}_{-0.4}$
SIS FOV	493.8/465	$3.2^{+0.4}_{-0.5}, 2.1 \pm 0.3^*$	$0.76^{+0.05}_{-0.04}$	11.2 ± 0.1	1.5 ± 0.2

* Extra N_{H} for the SIS.

Table 3. Emission measure ($n_e^2 L$) for each region of 3C400.2.

	NW	Center	SE
$n_e^2 L$ [$\text{cm}^{-6} \text{pc}$]	0.21 ± 0.03	0.14 ± 0.02	$0.058^{+0.006}_{-0.008}$
$n_e^2 L / (n_e^2 L)_{\text{SE}}$	3.6 ± 0.6	2.5 ± 0.5	(1.0)

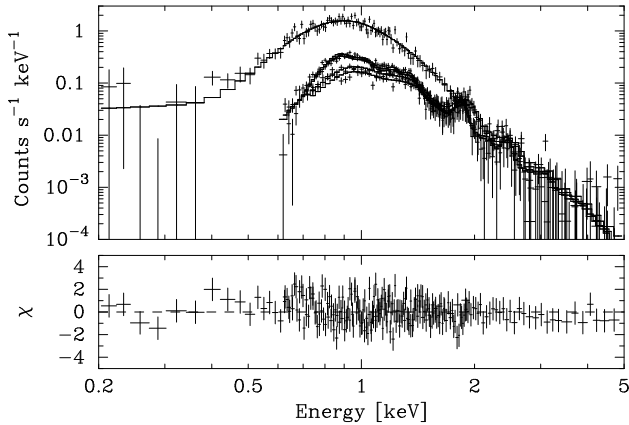


Fig. 4. Top panel showing the SIS 0, SIS 1, GIS 2, GIS 3, and PSPC spectra extracted from the SIS FOV. The lower panel shows the residuals of the fit for only SIS 0 and PSPC. The solid line is the best-fit model of case 3 (see table 2).

SIS FOV. The obtained spectra are shown in figure 4. Since it has been reported that SIS spec-

tra tend to show a higher value of the column density (ASCA Guest Observer Facility's home page at http://heasarc.gsfc.nasa.gov/docs/asca/cal_probs.html; Orr et al. 1998), we added an extra absorption feature for the SIS to the model of case 3. The results are listed in the bottom of table 2, and are consistent with those of the GIS/PSPC spectral fitting.

4. Discussion

As mentioned above, 3C 400.2 shows a unique morphology like two overlapping shells in radio. The mechanism which produces this morphology has been investigated in previous papers (Dubner et al. 1994; Saken et al. 1995; Giacani et al. 1998). We discuss it based on our results of the spectral fitting. The most interesting hypothesis is that 3C 400.2 consists of two interacting SNRs.

Bodenheimer et al. (1984) has carried out two-dimensional numerical calculations of the interacting of two SNRs in a uniform-density interstellar medium (ISM) with 1 cm^{-3} . They performed calculations while varying

Table 4. Parameters of 3C 400.2 and other mixed-morphology SNRs.

	3C 400.2	3C 391	W 44	W 28
Size [pc ²]	$(44 \times 35) D_5^{2*,\dagger}$	$21 \times 18^\ddagger$	$29 \times 17^\S$	$24 \times 24^\P$
kT_e [keV]	$0.8_{-0.1}^{+0.2}$	0.5^\ddagger	0.88^\S	2.0^\P
n_e [cm ⁻³]	$(0.05 \pm 0.01) D_5^{-1/2}$	0.63^\ddagger	0.42^\S	0.13^\P
E_t [erg]	$(5.6 \pm 1.4) D_5^{5/2} \times 10^{49}$	6.1×10^{49}	7.7×10^{49}	$2.6 \times 10^{50\text{P}}$
M_X [M_\odot]	$(38 \pm 7) D_5^{5/2}$	74^\ddagger	56^\S	27^\P

* D_5 is the distance in units of 5 kpc.

† $30' \times 24'$ (Saken et al. 1995)

‡ Rho and Petre (1996)

§ Harrus et al. (1997)

¶ Long et al. (1991)

the time interval and distance between the two supernova (SN) explosions. The morphology, which resembles that of 3C 400.2, was obtained in the case that the second SN explodes in the expanding shell of the first SN. The second SN explosion occurs 1.37×10^4 yr after the first SN. They calculated the X-ray intensity distribution at 1 keV, which shows a centrally peaked and non-spherical morphology at 8.7×10^4 yr after the first SN. Furthermore, they presented the evolution of the density and the temperature. Their simulation indicates a large temperature variation of $\sim 10^4$ from the center toward the shell. However, our analysis of 3C 400.2 indicates no variation of the temperature within the X-ray emitting region. Therefore, we conclude that the interaction of two SNRs does not reproduce the case of 3C 400.2. Saken et al. (1995) drew the same conclusion from the lack of a large temperature variation across the remnant with only the ROSAT PSPC data.

In addition, we investigated the possibility that the morphology of 3C 400.2 arises from two SNRs which are not interacting, but which are projected along the same line of sight. In this case, $n_e^2 L$ in the region where two shells are overlapping would become the sum of $(n_e^2 L)_{\text{NW}}$ and $(n_e^2 L)_{\text{SE}}$. At least, we would expect that the “center region” has a larger value of $n_e^2 L$ than other regions. Nevertheless, we could find no evidence of an excess value of $n_e^2 L$ in the “center region”, as shown in table 3. The hypothesis of the projection effect cannot apply to 3C 400.2.

Since it is unlikely that 3C 400.2 consists of two SNRs, whether they are interacting or not, we consider the case that it is a single SNR. Rho and Petre (1998) proposed that 3C 400.2 belongs to a class of “mixed-morphology SNRs”. They distinguish “mixed-morphology SNRs” from others with the following criteria. They are classified as a shell-type SNR at radio wavelength, while the

X-ray morphology is centrally peaked or amorphous. The X-ray emission is thermal emission from the ISM, not from the ejecta. In addition, there is no prominent, central, compact source in radio and X-ray bands. Based on these criteria, they give 7 SNRs as prototypical mixed-morphology SNRs. Besides 3C 400.2, it includes W 28, W 44, Kes 27, MSH 11–61A, 3C 391, and CTB 1.

In order to obtain the mean value of parameters over 3C 400.2, we performed a spectral fitting of the summed data of three regions for the GIS and the PSPC. The condition of the spectral fitting is the same as in case 3 for each region. The obtained best-fit values are consistent with those given in table 2. Using these values, we calculated the electron density (n_e), the thermal energy (E_t), and the mass of X-ray emitting material (M_X). The remnant is assumed to be an ellipsoid with two axes of $30'$ and $24'$ in the plane of the sky (Saken et al. 1995), and the depth which is equal to the length of a minor axis, $24'$. We also assumed the volume-filling factor to be unity and that the mean number density of hydrogen is equal to that of electrons, for simplicity. The results are given in table 4, where D_5 is the distance in units of 5 kpc. In addition, we have also listed the parameters for three other remnants among prototypical mixed-morphology SNRs, 3C 391, W 44 and W 28. At the writing phase of this paper, we could pick up the parameters of these three SNRs from the literature in order to compare 3C 400.2. We excluded CTB 1 from our list, since it has a complicate structure, as mentioned in section 1. The properties of 3C 400.2 are similar to those of 3C 391 and W 44, except for the electron density. The higher kT_e and the larger E_t of W 28 may be due to the contribution of non-thermal emission detected with the ASCA observation (K. Torii 1995, private communication).

A centrally peaked X-ray morphology observed in mixed-morphology SNRs cannot be derived from the Se-

dov (1959) similarity solution for a point explosion in a uniform-density ISM. Rho and Petre (1998) gave two most likely models which can explain the properties of mixed-morphology SNRs. One is a model in which the plasma at a shell has cooled to below $\sim 10^6$ K and its emission cannot be detectable in X-rays. The interior of the remnant is still hot due to a lower density than that at the shell. In this case, the plasma inside the shell must come from the ejecta, just as observed in the Cygnus Loop (Miyata et al. 1998). However, it is inconsistent with cosmic abundances observed across 3C 400.2.

An alternative explanation is the cloud evaporation model (White, Long 1991 and references therein). In this model, it is assumed that there are small and numerous cloudlets embedded in the ISM. These clouds have a much higher density than that of the tenuous and hot ISM. Therefore, they would not be accelerated by the passage of a shock wave. The clouds remaining in the interior of the shell gradually evaporate and emit X-rays. The thermal energy listed in table 4 represents the energy given to clouds by a shock wave. Long et al. (1991) found that the Einstein observation of 3C 400.2 can be explained by this model. We note that the important point in the cloud evaporation model is the presence of numerous, small and dense cloudlets in the environment of a SNR.

Among mixed-morphology SNRs, the most interesting object is 3C 391, with respect to the similarity to 3C 400.2. 3C 391 shows an elliptical shape with elongation from the northwest to the southeast, which resembles the morphology of 3C 400.2. In the radio band, a “breakout” structure is also seen in the southeast (Reynolds, Moffett 1993). Based on the radio and X-ray observations, Rho and Petre (1996) suggest that 3C 391 is the result of an explosion near to the edge of the molecular cloud. When the shock wave reaches the cloud boundary, a breakout would occur. Moreover, it is likely that there are numerous, small and dense cloudlets, which are required in the cloud evaporation model, at the edge of the molecular cloud. The CO observations confirmed the association between 3C 391 and a molecular cloud (Wilner et al. 1998).

In the case of 3C 400.2, Giacani et al. (1998) identified a dense HI cloud, which they argued is associated with 3C 400.2. In particular, the HI cloud surrounds the north and western side of the radio shell in the velocity range $+16.5$ to $+28$ km^{-1} . As Giacani (1998) proposed, a shock front propagating toward the southeast would meet a lower density medium and form the large shell by a breakout. Therefore, the morphology of 3C 400.2 can also result from an explosion occurring near to the edge of the HI cloud, as well as the case of 3C 391. This scenario can explain both the elongated radio morphology and the centrally peaked X-ray emission. As shown in table 2, the larger value of N_{H} in the NW region may in-

dicate the density gradient, though it is not clear due to large errors. Rho and Petre (1998) reported that most of mixed-morphology SNRs are interacting with molecular or HI clouds. Follow-up observations, such as a detailed CO mapping in the vicinity of 3C 400.2 or the detection of shock-excited OH maser emission, would be useful to confirm the interaction between 3C 400.2 and the cloud.

5. Conclusion

We performed a spectral analysis of 3C 400.2 with the ASCA and the ROSAT PSPC data. For all regions of 3C 400.2, we obtained a good fit by employing the NEI plasma model with cosmic abundances, except for a slight enhancement of Fe. No significant variation in the electron temperature and the ionization parameter was found across the entire remnant with $kT_e \sim 0.8$ keV and $\log \tau \sim 11$. On the other hand, the emission measure ($n_e^2 L$) tends to be larger from the southeast to the northwest. We therefore conclude that 3C 400.2 does not consist of two SNRs; nevertheless, the radio morphology of 3C 400.2 seems to be an overlapping of two shells.

We compared the values of kT_e , n_e , E_t , and M_X between 3C 400.2 and other prototypical mixed-morphology SNRs. Although n_e for 3C 400.2 is smaller than those of 3C 391 and W 44, other parameters show similar values. Based on these similarities and the existence of a dense HI cloud, we conclude that the morphology of 3C 400.2 is most easily explained in terms of a supernova explosion near to the edge of the cloud and a cloudlet evaporation model for the SNR.

We are grateful to all the members of the ASCA team. K.Y. is supported by JSPS Research Fellowship for Young Scientists.

References

- Agrawal, P.C., Riegler, G.R., & Singh, K.P. 1983, *Ap&SS*, 89, 279
- Allakhverdiev, A.O., Guseinov, O.Kh., Kasumov, F.K., & Iusifov, I.M. 1983, *Ap&SS*, 97, 287
- Anders, E., & Grevesse, N. 1989, *Geochim. Cosmochim. Acta*, 53, 197
- Bodenheimer, P., Yorke, H.W., & Tenorio-Tagle, G. 1984, *A&A*, 138, 215
- Case, G.L., & Bhattacharya, D. 1998, *ApJ*, 504, 761
- Caswell, J.L., & Lerche, I. 1979, *MNRAS*, 187, 201
- Clark, D.H., & Caswell, J.L. 1976, *MNRAS*, 174, 267
- Craig W.W., Hailey C.J., & Pisarski R.L. 1997, *ApJ* 488, 307
- Dotani, T., Yamashita, A., Ezuka, H., Takahashi, K., Crew, G., Mukai, K., & the SIS team 1997, *ASCA News*, 5, 14
- Dotani, T., Yamashita, A., Rasmussen, A., & the SIS team 1995, *ASCA News*, 3, 25
- Dubner, G.M., Giacani, E.B., Goss, W.M., & Winkler, P.F. 1994, *ApJ*, 108, 207
- Giacani, E.B., Dubner, G., Cappa, C., & Testori, J. 1998, *A&AS*, 133, 61
- Goss, W.M., Siddesh, S.G., & Schwartz, U.J. 1975, *A&A*, 43, 459
- Harrus, I.M., Hughes, J.P., Singh, K.P., Koyama, K., & Asaoka, I. 1997, *ApJ*, 488, 781
- Ishisaki, Y. 1996, Ph.D. thesis, The University of Tokyo
- Ishisaki, Y., Ueda, Y., Kubo, H., Ikebe, Y., Makishima, K., & the GIS team 1997, *ASCA News*, 5, 26
- Liedahl, D.A., Osterheld, A.L., & Goldstein, W.H. 1995, *ApJ*, 438, L115
- Long, K.S., Blair, W.P., White, R.L., & Matsui, Y. 1991, *ApJ*, 373, 567
- Masai, K. 1984, *Ap&SS*, 98, 367
- Mewe, R., Gronenschild, E.H.B.M., & van den Oord, G.H.J. 1985, *A&AS*, 62, 197
- Milne, D.K. 1979, *Austral. J. Phys.* 32, 83
- Miyata, E., Tsunemi, H., Kohmura, T., Suzuki, S., & Kumagai, S. 1998, *PASJ*, 50, 257
- Morrison, R., & McCammon, D. 1983, *ApJ*, 270, 119
- Nishiuchi, M., Yokogawa, J., Koyama, K., & Hughes, J. P. 2001, *PASJ*, 53 in press
- Orr, A., Yaqoob, T., Parmar, A.N., Piro, L., White, N.E., & Grandi, P. 1998, *A&A*, 337, 685
- Reynolds, S.P., & Moffett, D.A. 1993, *AJ*, 105, 2226
- Rosado, M. 1983, *Rev. Mexicana Astron. Astrofis.*, 8, 59
- Rosado, M., Laval, A., Boulesteix, J., Georgelin, Y.P., Greve, A., Marcelin, M., Coarer, E.Le, & Viale, A. 1990, *A&A*, 238, 315
- Rho, J.-H., & Petre, R. 1996, *ApJ*, 467, 698
- Rho, J.-H., & Petre, R. 1998, *ApJ*, 503, L167
- Saken, J.M., Long, K.S., Blair, W.P., & Winkler, P.F. 1995, *ApJ*, 443, 231
- Sedov, L.I. 1959, *Similarity and Dimensional Methods in Mechanics* (New York: Academic Press)
- Ueda, Y., Takahashi, T., Inoue, H., Tsuru, T., Sakano, M., Ishisaki, Y., Ogasaka, Y., Makishima, K. et al. 1999, *ApJ*, 518, 656
- White, R.L., & Long, K.S. 1991, *ApJ*, 373, 543
- Williams, R.M., Chu, Y-H., Dickel, J.R., Beyer, R., Petre, R., Smith, R.C., & Milne, D.K. 1997, *ApJ*, 480, 618
- Williams, R.M., Chu, Y-H., Dickel, J.R., Petre, R., Smith, R.C., & Tavarez, M. 1999, *ApJS*, 123, 467
- Wilner, D.J., Reynolds, S.P., & Moffett, D.A. 1998, *AJ*, 115, 247
- Winkler, P.F., Olinger, T.M., & Westerbeke, S.A. 1993, *ApJ*, 405, 608
- Yamauchi, S., & Koyama, K. 1993, *ApJ*, 404, 620
- Yoshita, K., Miyata, E., & Tsunemi, H. 2000, *PASJ*, 52, 867